FINITE ELEMENT SOLUTION OF THE EQUATIONS GOVERNING THE FLOW OF ELECTROLYTE IN CHARGED MICROPOROUS MEMBRANES

A. E. JAMES

Department of Chemical Engineering, UMIST, PO Box 88, Manchester, U.K.

AND

J. D. STILLMAN and D. J. A. WILLIAMS

Department of Chemical Engineering, University of Wales Swansea, Swansea SA2 8PP, U.K.

SUMMARY

Electrical double-layer effects are unimportant in flows through porous media except when the Debye length κ^{-1} is comparable in magnitude with the pore radius a. Under these conditions the equations governing the flow of electrolyte are those of Stokes, Nernst–Planck and Poisson. These equations are non-linear and require numerical solution. The finite element method provides a useful basis for solution and various algorithms are investigated. The numerical stability and errors of each scheme are analysed together with the development of an appropriate finite element mesh. The electro-osmotic flow of a typical electrolyte (barium chloride) through a uniformly charged cylindrical membrane pore is investigated and the ion fluxes are post-computed from the numerical solutions. The ion flux is shown to be strongly dependent on both zeta potential and pore radius, κa, indicating the effects of overlapping electrical double layers.

KEY WORDS   electrolyte flow; finite element method; non-linear

1. INTRODUCTION

Membranes are of great utility in many industrial separation processes. In water treatment they may be used for purification by removing unwanted ionic species and fine particles, while in biological processes they may be used to concentrate a chosen ionic species or solid of commerical value.

Typically a membrane allows the passage of an aqueous electrolyte through capillary pores with submicron equivalent diameters. The capillary pores may be produced by the irradiation of sheets of polymer or the packing of fine fibres or particles in a suitable assembly.[1] Electrolyte flow through membranes is a complex process, being influenced not only by the diameter of the capillary pore but also by the membrane material and the ions present within the electrolyte.[1-5] Further complications are introduced by the presence of dispersed colloidal material. Electrolyte flow through a membrane may be driven either by pressure or by an electrical potential. Thus it is self-evident that improved design and operational procedures for membrane separation processes can only result from fundamental understanding of the chemical physics of the electrolyte flows on length scales appropriate to membranes.

In the presence of an aqueous electrolyte, membranes can possess a surface electrical charge which will give rise to the formation of an electrical double layer caused by the dynamical partition of ions of similar and dissimilar charge to the surface. Discussions of the origin of this charge and the absorption of the lyaer of ions onto the charged surface (the Stern layer[2,3]) are beyond the scope of the present study and readers are referred to standard texts on colloid science.[2,3] Outside the layer of bound ions the diffuse electrical double layer develops, the extent of which is characterized by the Debye length κ^{-1} (defined by equation (10)). The Debye length is a function of ionic charge and concentration and typicall $\kappa^{-1} < 1000$ Å. The diffuse double layer is mobile and for electrokinetic flows the transition between the fixed and mobile layers is termed the slippig plane.[2] The notion of the existence of the slipping plane provides a suitable datum for both hydrodynamic and electrical boundary conditions. In flows through porous media the existence of the electrical double layer is unimportant when the ratio of the electrical double-layer thickness to the pore radius is much less than unit. However, when this ratio is $O(1)$, the double layers start to overlap, giving rise to an electroviscous effect. Further, when the capillary radius is small compared with κ^{-1}, the possibility of ion rejection exists and flux of certain ions through the membrane will be reduced.

Comparatively little theoretical attention has been given to the analysis of electrolyte flows in membranes,[1] which requires the solution of a complex set of differential equations for the simplest model system.[4,5] Analytical solutions are possible, but the severe restrictions necessary in their formulation limit their usefulness in the prediction of flow characteristics.[5-10] Preliminary studies of the effects of pore shape have been made using a combination of analytical and collocation meethods.[11,12] Although these studies were restricted to binary symmetrical electrolytes with uniform ionic mobility and uniform surface charge distribution, some allowance for non-uniformity of the pore wall was made by allowing a periodic variation in the surface charge. An obvious shortcoming in the majority of previous investigations is the neglect of the more intriguing aspects of real electrolyte flows. Studies should recognize that some electrolytes are asymmetric while others are complex mixtures of ions, each having its own ionic mobility. The effects of a non-uniform distribution of charge and variable pore shape should be considered in more detail. In contrast with earlier work, we consider a flexible numerical scheme that may be used for detailed investigation of electrolyte flow in charged pores where non-uniform distributions of material properties and irregular geometry are of special interest. The equations governing electrolyte flow are those of Stokes, Poisson and Nernst–Planck (NP).[4] These equations are strongly non-linear, although the Stokes and Poisson equations are linear if the space charge density ρ is constant. In general, numerical methods of solution are necessary.

The present study describes the formulation of a finite element algorithm to solve the governing equations of electrolyte flow within a charged porous membrane. Lagrange finite elements are used in a Galerkin discretization. The resultant sets of non-linear equations are solved by iterative methods. The limitations on mesh size and the magnitude of the non-linearity through the boundary conditions are investigated. A series of simple test cases is used to validate the numerical model. Electrolyte flows and ion fluxes are calculated within a typical membrane pore and are applicable to electrolyte solutions of concentration less than 0·5 M.

NUMERICAL ANALYSIS

The governing equations are

$$N^h = -d^h \nabla c^h = -\frac{z^h e}{kT} d^h c^h \nabla \varphi + c^h v \quad \text{(NP)}, \tag{1}$$

$$\nabla^2 \varphi = -\rho \varepsilon \quad \text{(Poisson)}, \tag{2}$$

$$-\nabla p + \rho \nabla \varphi - \mu \nabla \times \nabla \times v = 0 \quad \text{(Stokes)} \tag{3}$$

and closure of equations (1)–(3) requires

$$\nabla \cdot N^h = 0 \quad \text{(conservation of ion flux)}, \tag{4}$$

$$\nabla \cdot v = 0 \quad \text{(conservation of volume)}, \tag{5}$$

$$\nabla \cdot (\varepsilon E) = 0 \quad \text{(conservation of electrical flux density)}, \tag{6}$$

where N^h, d^h, c^h and z^h are the flux, diffusivity, concentration and valency (with the sign of the charge included) of ionic species h respectively, k is Boltzmann's constant, T is the absolute temperature, e is the electronic charge, v is the velocity, ε is the permittivity, E is the electrical field vector, φ is the total electrical potential in the pore, p is the pressure and μ is the bulk viscosity.

In order to illustrate the method adopted, we develop a numerical solution for dlectrokinetic flow within a charged cylindrical membrane pore in cylindrical co-ordinates. The pore is one of many whose axes are normal to the membrane face. A difference in voltage applied across the membrane produces an electrical field, inducing flow parallel to the axis of the pore. This electrical field vector contains only an axial component, so that the electrical potential within the pore is written as

$$\varphi(z, r) = \psi(z, r) + z E_z, \tag{7}$$

where z is the distance along the pore axis (see Figure 1), ψ is the electrostatic potential within the electrical double-layer system and E_z is the axial electrical field. The space charge density ρ within the pore is determined as

$$\rho = N_A e \sum_h z^h c^h(z,\ r,\ \varphi), \tag{8}$$

where N_a is Avogadro's number. For a pore radius a when the double layer is thin ($\kappa^{-1} << a$), bulk values of viscosity and concentration are expected along the axis of the pore as well as in the external electrolyte, since there is no overlap of the double layers within the pore. When κ^{-1}, the electrical double layers overlap and the ionic concentration will vary from the bulk value as predicted by the NP equation (1). In this instance the overlapping double layers also induce an apparent increase in viscosity, evident in reduced volumetric flow rates through the pore, which is known as the electroviscous effect.[7]

The ionic strength I of the bulk electrolyte is a function of the bulk ionic concentrations and valencies of the individual ionic species and is given by

$$I = \tfrac{1}{2} \sum_h (z^h)^2 c^h(\infty), \tag{9}$$

where $c^h(\infty)$ is the bulk concentration of ionic species h. The Debye length κ^{-1} is written as a function of I:

$$\kappa^{-1} = \left(\frac{2 N_A I e^2}{\rho k T} \right)^{-1/2}. \tag{10}$$

It is now convenient to define

$$C^h = \frac{c^h}{I}, \qquad \Psi = \frac{e\psi}{kT}, \qquad V = \frac{\kappa \mu}{kT N_A I}\, v = \frac{v}{\beta_\varepsilon}, \qquad P = \frac{1}{kT N_A I}\, p, \tag{11}$$

$$R = \kappa r, \qquad Z = \kappa z, \tag{12}$$
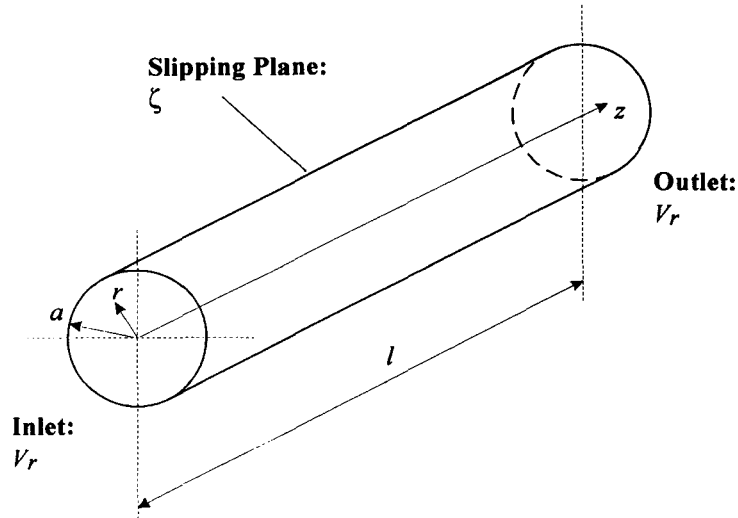
Figure 1. Uniformly charged capillary

where β_ε is the characteristic velocity scale of the flows in the electrical double-layer system in the present work.

Further, the non-dimensional form of equation (7) for the total electrical potential in the pore is written as

$$\Phi(Z,R) = \Psi(Z,R) - ZE_z, \tag{13}$$

where $E_z = (e/\kappa kT)E_z$.

Introducition of the dimensionless quantities into equations (1)–(3) and (5) and substitutions of equation (1) into equation (4) allows one to write the working equation set as

$$-\nabla^2 C^h - z^h(\nabla C^h \cdot \nabla\Phi + C^h\nabla^2\Phi) = \frac{\beta_\varepsilon}{\kappa d^h} V \cdot \nabla^2 C^h = 0 \quad \text{(NP)}, \tag{14}$$

$$\nabla^2\Psi = -\tfrac{1}{2}\sum_h z^h C^h \quad \text{(Poisson)}, \tag{15}$$

$$-\nabla P + \sum_h z^h C^h \nabla\Phi - \nabla \times \nabla \times V = 0 \quad \text{(Stokes)}, \tag{16}$$

$$\nabla \cdot V = 0 \quad \text{(conservation of mass)}. \tag{17}$$

In equation (4), $\beta_\varepsilon/\kappa d^h$ is a Peclet number (Pe) indicating the relative importance of convection and conduction within the ion fluxes. We have found in general that $Pe, 1$, indicating a dominance of ion movement through diffusive conduction in the systems under study. However, values of Pe are not sufficiently small to warrant neglect of the convective terms in the ion flux equations.

The electro-osmotic flow is determined by solution of equations (13)–(17) subject to the boundary conditions

$$Z = 0: \quad V_r = 0, \quad \frac{\partial V_z}{\partial Z} = 0, \quad \frac{\partial C^h}{\partial Z} = 0, \quad \frac{\partial \Psi}{\partial Z} = 0, \quad \frac{\partial \Phi}{\partial Z} = -E_z,$$

$$Z = \kappa l: \quad V_r = 0, \quad \frac{\partial V_z}{\partial Z} = 0, \quad \frac{\partial C^h}{\partial Z} = 0, \quad \frac{\partial \Psi}{\partial Z} = 0, \quad \frac{\partial \Phi}{\partial Z} = -E_z,$$

$$R = 0: \quad V_r = 0, \quad \frac{\partial V_r}{\partial R} = 0, \quad \frac{\partial C^h}{\mathrm{d}R} = 0, \quad \frac{\partial \Phi}{\partial R} = 0,$$

$$R = \kappa a: \quad V_z = 0, \quad V_r = 0, \quad \Psi = \frac{e\zeta}{kT}, \quad C^h(\kappa a, Z) = C^h(\infty) \exp\left(-\frac{z^h e\zeta}{kT}\right),$$

where ζ is the electrical potential at the slipping plane and $C^h(\infty)/I$. The last boundary condition for the ion concentration at the slipping plane ($C^h(\kappa a, Z)$) is obtained by integrating the radial component of equation (1) at $r = a$, noting that $N_r^h(a,z) = 0$ and $v_r(a,z) = 0$, and expressing the result in non-dimensional parameters.

In the present work the governing equations are discretized and the resultant non-linear algebraic equations are solved iteratively. In order to work, this procedure requires some *as priori* knowledge of the distribution of ions within the pore. Evidently a likely initial condition would be the assumption of a uniform distribution of ions throughout the pore; in practice, however, it is more convenient to assume a Boltzmann distribution of ions with respect to the wall within the pore. Consequently the Poisson equation becomes the Poisson–Boltzmann (PB) equation, which is written non-dimensionally as

$$\nabla^2 \Psi = -\frac{1}{2} \sum_h z^h C^h(\infty) \exp\left(-z^h \Psi\right) \tag{18}$$

and is subject to the boundary conditions

$$Z = 0 \text{ and } Z = \kappa l: \quad \frac{\partial \Psi}{\partial Z} = 0, \qquad R = 0: \quad \frac{\partial \Psi}{\partial R} = 0 \qquad R = \kappa a: \quad \Psi = \frac{e\zeta}{kT}.$$

The PB equation is also non-linear and must be solved using the Newton-Raphson (NR) method.[13] A trial solution to initiate the Newton sequence is obtained by solving the Debye–Hückel (DH) linearization of the PB equation. This is obtained by expanding the exponential term in equation (18), neglecting terms in Ψ^2 and above and remembering that the overall electroneutrality of the bulk electrolyte demands that $\sum_h z^h C^h(\infty) = 0$.. In the present work the linearized form is termed the DH–Poisson (DH–P) equation and is written as

$$\nabla^2 \Psi = \Psi \tag{19}$$

Equations (14)–(19) subject to their respective boundary conditions are the basis for our model of electrolyte flow through porous membranes. Their numerical solution can now be presented.

FINITE ELEMENT PROCEDURES

The Galerkin finite element method (FEM)[14] is used to discretize equations (14)–(19). Since there are no unusual features in the FE methodology used in the present study, the element matrix equations can be readily determined and will not be presented therein. Similarly the global assembly and matrix solution algorithms are well documented and do not warrant detailed examination. For convenience

hereafter, we call the finite element discretization of a particular differential equation by the name of the parent differential equation. Unless otherwise stated, we refer to fully assembled global matrix equations into which have been introduced both essential and natural boundary conditions. We have used nine-noded Lagrangian finite elements to form the element matrices of the DH–P, PB, Poisson and NP equations. The Stokes and mass conservation equations are discretized using the so-called primitive variables method[15] on noded Lagrangian elements (for velocity) with superimposed four-noded linear elements (for pressure). Various authors have shown that this combination of elements together with the primitive variables methodology can be readily applied in the successful solution of a broad range of Navier–Stokes flow problems.[16,17] Weakened pressure gradient terms enable the straightforward specification of pressure at any location.[18] Picard iteration has been used to solve all the equations except the PB equation, which is solved by the Newton–Raphson (NR) method. The quasi-linearization of this equation and the use of Newton sequences in the subsequent solution of the linearized matrix equations have been fully described elsewhere.[19] The global matrices are inverted using a frontal solver.

VALIDATION OF GOVERNING EQUATIONS

Herein numerical solutions of each differential equation (Stokes, DH–P, PB, Poisson and NP) are compared with an appropriate analytical result. For convenience we consider the binary symmetrical electrolyte whose properties are given in Table I.

Figure 1 illustrates the test geometry and required boundary conditions. To investigate the effects of element size, a range of FE meshes employing Lagrange elements and 10, 50 or 100 equal radial divisions is used. The results obtained for each equation are summarized below.

Stokes equation

This is solved with respect to the boundary conditions ($V = 0$ at slipping plane, $\partial V_r/\partial R = 0$ at capillary axis). The electrical field is set to zero and a pressure difference applied across the pore drives the flow. Comparison is made between the axial velocity component of the FE solution under these conditions and the theoretical parabolic profile written in dimensionless variables as

$$V_z(R) = V_z^{max}\left[1 - \left(\frac{R}{\kappa a}\right)^2\right],\tag{20}$$

where V_z^{max} is the velocity at the axis of the pore. Under creeping flow conditions the solution to equation (16) matches that of equation (20) within the accuracy of computer word length on all meshes.

Poisson, Poisson–Boltzmann and DH-Poisson equations

The numerical solution of these equations is sensitive to the magnitude of both $e\zeta/kT$ and κa. For low slipping plane potentials $(e\zeta/kT << 1)$ in narrow capillaries the solution of equation (19) is

Table I. Properties of binary symmetrical electrolye

Positive ions			Negative ions		
Concentration (kmol m^{-3})	Valency	Mobility (cm^2 s^{-1} V^{-1})	Concentration (kmol m^{-3})	Valency	Mobility (cm^2 s^{-1} V^{-1})
1×10^{-4}	1	5×10^{-4}	1×10^{-4}	1	5×10^{-4}

similar to that of equation (18). Herein 25 mV is taken to the limiting value of ζ for similar solutions to equations (18) and (19) (i.e. $e\zeta/kT = 1$) and this value was used for test purposes with pores having radii $\leq 0 \cdot 05$ μm.

The radial solution of equation (19) for a long, uniformly charged cylindrical pore is given in terms of Bessel functions as[13]

$$\Psi_B = \frac{e\zeta}{kT}\frac{I_0(\kappa r)}{I_0(\kappa a)},$$

(21)

where $I_0()$ is a Bessel function of the second kind, calculated in the present work from the algorithms presented by Abramowitz and Stegun.[20]

Numerical values of Ψ_B deterimed by equation (21) are exact to six significant figures. Within the bounds of stability (discussed later) the solution to equation (19) always exceeds this resolution. Comparisons of results from equation (21) with those from equations (18) and (19) are interesting in that the solutions differ by a maximum pointwise value of 3·47% in a capillary with radius $a = 0 \cdot 05$ μm.

This value is maintained irrespective of the degree of radial mesh refinement, indicating the correctness of the numerical solution.

Nernst–Planck equation

For a long cylinder it is possible to analytically solve the radial component of the NP equation. The required solution is obtained under conditions where there is no hydrodynamic flow (i.e. $V = 0$). The subsequent integration (13) is straightforward subject to the boundary condition $C_h = C_h(\infty)$ when $\Psi = 0$:

$$C^h = C^h(\infty)e^{-z\Psi}.$$

(22)

Equation (22) predicts a Boltzmann distribution of ions in the radial direction. Insertion of equation (22) into the Poisson equation leads to an equation identical in form with the PB equation (18). A comparison between the results obtained for the PB equation and the solution to the NP equation in conjunction with both the Stokes and Poisson equations provides an estimate of the accuracy of the coupled equation set. Differences between the post-computed PB-based values for C^h and the values obtained from the NP equation exceed six-figure accuracy, thus verifying the NP equation under the test conditions.

From the above illustrative solutions we were able to conclude that subject to the limitations of arithmetic precision and numerical stability our modelling of each individual equation has been successful. We now present solution algorithms for the electrolyte flow in charged cylindrical pores using equations (13)–(17).

SOLUTION ALGORITHM

Two distinct strategic for solution are suggested. The first, which is confined to infinitely long capillaries, requires only the PB and Stokes equations, the initial distribution of potential for the PB equation being obtained from the DH–P equation. The second, which is generally applicable to all geometries, uses the governing equations (13)–(19). The first method is computationally less expensive. Since it does not require the solution of at least two extra ionic transport equations, and would appear to hold a distinct advantage over the second method. The authors have found that in instances of strong non-linearity, arising through a high slipping plane potential ζ and possibly in conjunction with large κa-values, the PB equation leads to numerically convergent results which are

erroneous. To assist in the identification of erroneous solutions, the following weighted residual norm[12] is independently applied to the solution variables:

$$\Omega^{\mathrm{norm}} = \frac{1}{NH} \sum_{1}^{nh} (\alpha^n - \alpha^{n-1^2}),\tag{23}$$

where NH is the number of mesh nodes, $\alpha = [u, v, \Psi, C^h]^{\mathrm{T}}$ and n and $n-1$ denote the present and previous solutions respectively. Note that the pressure is not included in α since it is instantaneously satisfied function of the velocity field. Operationally, equation (23) is satisfied when $\Omega^{\mathrm{norm}} \leq 0 \cdot 0001$. Overall convergence within the programme is achieved when the norm is satisfied by all variables.

The two schemes are summarized below

PB–S scheme

1. Solve the DH–P equation for electrical potential using values of bulk concentration as initial values and the slipping plane potential as the electrostatic boundary condition.
2. Solve the PB equation for electrical potential.
3. Solve the Stokes (and mass conservation) equations for the velocity and pressure field using the electrical potential from step 2 and the external gradient E_2.
4. Continue with steps 2 and 3 until successive solutions for all variables converge.

NP–P–S scheme

1. Solve the DH–P equation for electrical potential using values of bulk concentration as initial values and the slipping plane potential as the electrostatic boundary condition.
2. Solve the PB equation for electrical potential.
3. Solve the Stokes (and mass conservation) equations for the velocity and pressure field using the electrical potential from step 2 and the electrical gradient E_Z.
4. Solve the NP equation for each ionic species for the total distribution of ionic concentration using velocities from step 3 and electrical potentials from step 2.
5. Solve the Poisson equation for electrical potential using ionic concentrations from step 4.
6. Continue with steps Steps 3–5 until successive solutions for all variables converge.

In practice, for solutions using the PB–S scheme with a slipping plane potential $\zeta = 50$ mV and dimensionless radius $\kappa a = 5$, convergence is achieved within 5–10 iterations. Using the NP–P–S scheme for the same binary electrolyte and converged values from the PB–S scheme as seed values requires an additional 10 iterations. This represents a computing overhead of about 100%. For problems with high non-linearity or an electrolyte with more than two ionic species or both the computational overhead can exceed 200%. Clearly the former scheme is computationally attractive; however, we subsequently demonstrate that the latter scheme is to be preferred because of its superior numerical performance, even in the present simple example of electrolyte flow in capillary pores of constant cross-sectional area.

RANGE OF ACCURACY AND ERROR DETERMINATION

To examine the numerical performance of each scheme, the bounds of model applicability are discussed and summary guidelines are supplied for any future implementation of the numerical algorithms. The effects of the two principal factors influencing the non-linearity of the equations, namely the slipping plane potential ζ and the dimensionless pore radius κa, are examined.

Electrokinetic data and mesh design for the numerical solution have been described previously in the section on model validation. The meshes used have equally spaced elements, since it was found that

concentrating a similar total number of elements near the slipping plane (in a similar manner to mesh designs used for NS transport problems[21]) does not offer any advantage—the overall accuracy is found to be reduced. Concentrating elements towards the centreline also results in a loss of some accuracy. Since large radial gradients do not exist in the geometries under consideration in the present study, no advantage is obtained by using graded meshes.

As κa is increased for a fixed number of radial elements, the solution either becomes numerically unstable or contains unacceptable errors which are manifested as oscillations in the potential distribution close to the slipping plane. The solution of the PB or Poisson equation has been identified in the present study as the primary source of numerical error. Within both numerical schemes the FE solutions of the Stokes equations and associated mass conservation equation perform satisfactorily at all times. Similarly the FE solution of the NP equation performs well and only oscillates when supplied with unsatisfactory values of electrical potential from the Poisson equation.

Instability in the PB–S scheme is first notices when the radial distributions of electrical potential are seen to possess nodal oscillations—although the solution satisfies convergence criteria. These nodal oscillations are unacceptable in the present problem, since the governing equations require a smooth decay of electrical potential away from the slipping plane. In instances where either or both slipping plane potential and dimensionless radius are large (typically $\zeta > 100$ mV and $\kappa a > 10$), a second regime of instability occurs.

Instability in the NP–P–S scheme differs from that described above. The FE solution of the Stokes, mass conservation and NP equations is dependent on the successful FE solution of the Poisson equation. Failure of the FE Poisson solution is readily observed as a divergence in successive iterations. In contrast with the visual examination necessary to identify nodal oscillations in the FE PB solution, the divergence in the FE Poisson solution is easily detected by the weighted error norm (equation (23)). In most circumstances the former equations produce apparently convergent solutions. In exceptional circumstances (again typically $\zeta > 100$ mV and $\kappa a > 10$) the FE solution to the NP equation diverges, accelerating the instability of the overall solution.

The onset of instability in the numerically solved electrolyte flow problems of the present study suggests a critical ratio between physical and modelling scales which can be expressed as

$$R_{crit} - \kappa a/NE_r, \qquad (24)$$

where NE_r is the number of radial elements.

The NP–P–S solution method fails to locate a solution when R_{crit} is reached; however, the PB–S solution method may appear to locate a solution, but examination of the pointwise potential values reveals the aforementioned oscillations. From the above discussion it is clear that the NP–P–S algorithm has inherently greater provision for reliable solutions. It has been shown previously (see section on model validation) that the potential distributions calculated from the PB or Poisson equation differ from the Bessel function solutions even at low slipping plane potentials. The maximum differences of the Poisson and PB equation solutions from the Bessel function solutions are identical until the onset of instability and this may be used as a convenient datum from which we can measure stability. The effect of uniformly increased radial mesh refinement corresponds to an extension of the range of solutions in the non-linear zone. Doubling the number of radial elements used produces a proportional increase in the ratio R_{crit} that can be examined. As an example, at $\zeta = 25$ mV R_{crit} has a value of 5.0×10^4 (a small margin of safety is included).

To graphically illustrate the applicability of the model in practical situations, the FE mesh with 50 equally spaced radial elements is used with various pore radii to examine the influence of slipping plane potentials on the scope of possible solution. Bands of stabel solutions for various values of slipping plane potential up to the limiting values of R_{crit} are shown in the stability diagram of Figure 2.
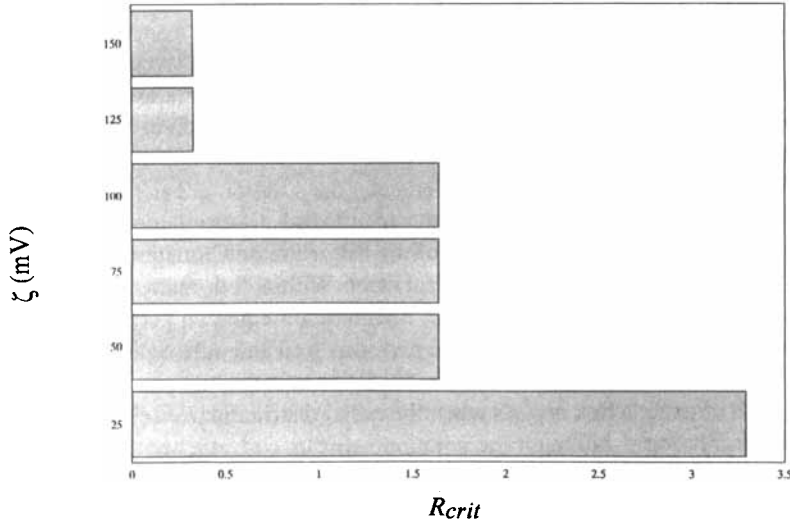
Figure 2. Stability diagram. The shaded area represents the extent of the stability offered by the numerical solution

In a previous study[19] an investigation of the absolute error in the FE solution of the PB equation suggests that

$$\omega = m'\xi^{2n'} \tag{25}$$

where ξ is the distance between adjacent FE nodes and m' and n' are constants that may be determined by comparing FE and exact solutions. In the absence of a more rigorous theory it is assumed that the simplest error estimate in the FE solutions developed herein is given by an expression of similar form to equation (25). In the present study there is no exact analytical solution which may be used as a basis of comparison. Consideration of the error in the FE solutions and the presumed exact solution with the aid of Figure 3 allows one to write

$$\omega = \omega_p + \omega_{fine}, \tag{26}$$

where ω_p is the difference between the fine and coarse mesh solutions and ω_{fine} is the error between the fine mesh FE solution and the exact solution.

Assuming that ω is determined from an expression analogous to equation (25), the difference between the fine and coarse mesh FE solutions is

$$\omega_p = m\xi^n\left[1 - \left(\frac{\xi_{fine}}{\xi}\right)^n\right], \tag{27}$$
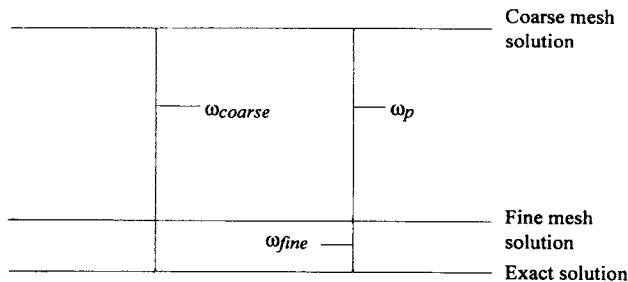
Figure 3. Schematic comparison of errors between coarse and fine FE solutions and the exact solution

where m and n are as yet undetermined constants and ξ_{fine} is the fine mesh internodal distance. In practice it is easy to choose ξ_{fine} so that $\xi/\xi \ll 1$, so that we may write

$$\omega_p \approx m\xi^n. \tag{28}$$

Equation (28) is used as the basis of subsequent error analysis. After taking logarithms, equation (28) is transformed to

$$\ln \omega_p = \ln m + n \ln \xi. \tag{29}$$

If our assumptions are true, then plotting $\ln \omega_p$ as a function of $\ln \xi$ should result in a straight line of slope n and with intercept $\ln m$ on the $\ln \omega_p$-axis.

A series of numerical experiments was performed wherein the mesh was systematically refined. The finest mesh was assumed to facilitate solution with least error and results using coarse meshes are compared with the fine mesh results. We choose potential as the variable for consideration, because velocity and concentration fields are linked through the governing equations. Figure 4 shows the variation in $\ln \omega_p$ with $\ln \xi$. The straight line gives experimental confirmation of our assumed model for the variation in error with internodal distance. The exponent n in equation (28) is found to be $1 \cdot 85$ and $m = 1 \cdot 46$. Equation (28) is fully satisfied and may be used to predict the order of the FE error. Use of the stability diagram in addition to use of the error estimates from equation (28) provides suitable controls for our subsequent numerical work.

NUMERICAL RESULTS

The NP–P–S algorithm is used to generate all the results. The geometry and boundary conditions have been previously defined in Figure 1. Barium chloride is used (see Table II) in all examples. Dimensionless radial distributions of potential, axial velocity and ionic concentration within a pore are presented for a range of ζ-values in Figures 5–6. Calculations of total and individual ionic fluxes through the pore for various ζ and κa-values are shown in Figure 7. The ionic strength from equation (9) is $1 \cdot 5 \times 10^{-4}$ M.

Herein results are presented for values $\zeta = -25, -75$ and -125 mV. The slipping plane is located at a dimensionless pore radius of $\kappa z = 4 \cdot 029$ and the axis is at $\kappa r = 0 \cdot 0$. Stability calculations show that a 100-element uniformly spaced radial mesh is required. The value of the applied field E_z, based on experimental observations[18] is 350 V m^{-1}.

Figure 5 shows the radial distribution of potential (Ψ) and axial velocity (V_z) within the pore for $\zeta = -25$ mV. The potential distribution is exponential, rising from $\Psi(\kappa a) = -0 \cdot 974$ to $\Psi(0) = -0 \cdot 892$. The velocity profile indicates that reverse flow is occurring in the centre of the pore and the velocity ranges from $V_Z(\kappa a) = 0 \cdot 0$ to $V_z(0) = -4 \cdot 054 \times 10^{-7}$. Evidently the electro-osmotic flow is not uniform across the entire pore, reflecting the effect of double-layer overlap which is neglected in simple double-layer theory.[2] Figure 6 shows the complementary radial distribution of dimensionless concentration within the pore. There is a marked difference in the distribution of cations and anions. The anionic concentration increases from $C^{-1}(\kappa a) = 0 \cdot 252$ to $C^{-1}(0) = 0 \cdot 273$, while

Table II. Properties of barium chloride

Cations			Anions		
Concentration (kmol m^{-3})	Valency	Mobility (cm^2 s^{-1} V^{-1})	Concentration (kmol m^{-3})	Valency	Mobility (cm^2 s^{-1} V^{-1})
5×10^{-5}	2	6·59	1×10^{-4}	1	7·91
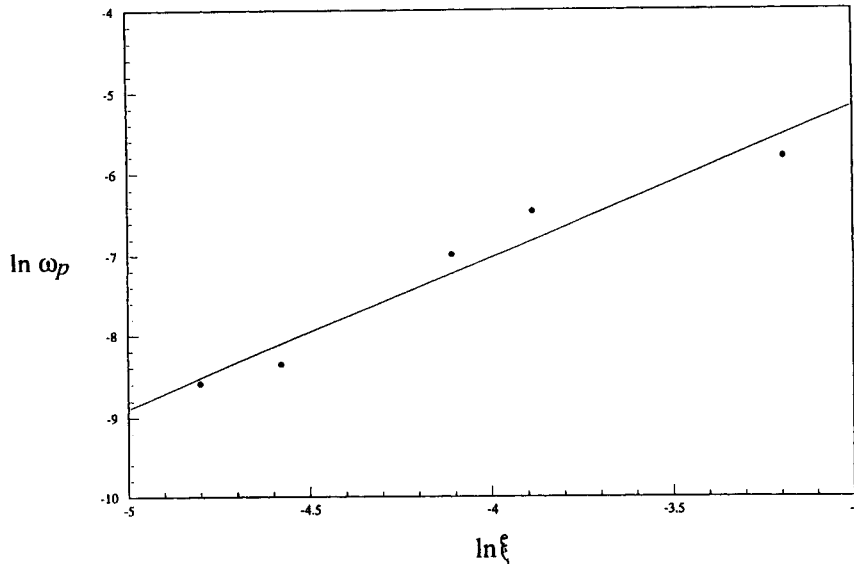
Figure 4. Relative error ω_p as a function of internodal distance

the cationic concentration decreases from $C^{+2}(\kappa a) = 2\cdot336$ to $C^{+2}(0) = 1\cdot985$. The dimensionless bulk concentration of anions, $C^{-1}(\infty) = 0\cdot667$, is not exceeded by the negatively charged ions across the whole of the pore. In contrast, the cationic concentration exceeds the bulk value $C^{+2}(\infty) = 0\cdot333$. It is apparent that there are significant differences in ionic concentration between the values predicted within the pore and those of the bulk electrolyte.

For $\zeta = -75$ mV (see Figure 5) the potential rises from $\Psi(\kappa a) = -2\cdot921$ to $\Psi(0) = -1\cdot946$ and the velocity falls from $V_z(\kappa a) = 0\cdot0$ to $V_z(0) = -6\cdot33 \times 10^{-5}$. The anionic concentration (see Figure 6) increases from $C^{-1}(\kappa a) = 0\cdot036$ to $C^{-1}(0) = 0\cdot0998$, while the cationic concentration falls from $C^{+2}(\kappa a) = 114\cdot75$ to $C^{+2}(0) = 14\cdot875$.

For $\zeta = -125$ mV (see Figure 5) the potential rises from $\Psi(\kappa a) = -4\cdot867$ to $\Psi(0) = -2\cdot115$ and the velocity falls from $V_z(\kappa a)$ to $0\cdot0$ to $V_z(0) = -2\cdot182 \times 10^{-4}$. The anionic concentration (see Figure 6) increases from $C^{-1}(\kappa a) = 0\cdot005$ to $C^{-1}(0) = 0\cdot080$, while the cationic concentration falls from $C^{+2}(\kappa a) = 5636\cdot416$ to $C^{+2}(0) = 22\cdot903$.

Consideration of the concentration profiles within the pore (Figures 5 and 6) shows that the space charge consists mainly of cations.

The transport of ions through a pore is determined by integrating the individual fluxes over the cross-sectional area. In particular, the total axial ionic flux f in a circular capillary may be found at any position along the axis using the expression

$$f = \sum_h f^h = 2\pi \sum_h \int_0^a N^h(r) r \, dr,$$

where $N^h(r)$ is post-computed using equaiton (1) and f^h is the total axial flux of ionic species h through the pore.

Specific ion fluxes are shown for a range of radii and zeta potentials in Figure 7. The range of slipping plane potentials investigated is $-25 \le \zeta \le -150$ mV. The results were produced using uniformly spaced radial meshes of varying refinement in accordance with the stability diagram (Figure 2). The curves illustrate the trend for ion transport through the pore. There is an inverse relationship

between the cation and anion fluxes at a particular ζ for any κa-value. Specifically, at a chosen value of κa, the higher the zeta potential, the greater is the cation flux and the smaller is the anion flux. The percentage cation flux (Table III) is calculated from

$$\Xi = 100\frac{f^{+2}}{f}. \tag{31}$$

Table III shows that at $\kappa a = 0.2$ there is a significant cationic flux at low zeta potential. This flux approaches 100% with increasing ζ. When $\kappa a = 0.0$, the cation flux is less pronounced at low ζ but replicates the earlier trend at higher ζ. Consideration of Figure 7 and Table III suggests that for negatively charged membranes the ion flux at given ζ is dependent on the degree of electrical double-layer overlap (i.e. κa).

Table III. Percentage of cations in total flux (to two decimal places)

ζ	Cation percentage			
	$\kappa a = 0.2$	$\kappa a = 2.0$	$\kappa a = 0.4$	$\kappa a = 0.4$
−25	88·18	87·22	72·62	58·51
−50	99·15	98·76	92·11	81·32
−75	99·92	99·81	97·56	92·51
−100	99·98	99·95	99·15	97·11
−125	100·00	99·99	99·69	99·03
−150	100·00	100·00	99·90	99·70

FINAL REMARKS

Electrolyte flow through membranes is a complex process dependent on pore geometry, membrane material, slipping plane potential and the mobilities of various ionic species present. Herein we have presented the equations governing electrolyte flow in a non-dimensional form suitable for numerical solution. In general the Peclet number for these flows is less than unity, indicating the dominance of ion mobility in the problems studied. The value of Pe is not sufficiently small to neglect the convection terms in the flux equations.

Of the various algorithms investigated, the NP–P–S scheme is found to be the most useful. In the PB–S scheme the assumption of a Boltzmann distribution of ions with respect to the wall is valid for a cylindrical pore and provides computational advantages. However, the PB–S scheme suffers from numerical instabilities and can exhibit an apparent but erroneous convergence, producing inappropriate results even for the ideal cylindrical geometry. Errors in the NP–P–S scheme was readily detected using the norm (equation (23)), and although computationally more expensive, this scheme is preferred.

Investigations into variable-sized element meshes indicate that at least for the present problem a regular FE mesh produces the best results. This is clearly an area for future work, especially when flows through more complex geometries are investigated.

The development of a diagram indicating the region of stability of the NP–P–S scheme together with a simple analysis of FE errors provides a useful framework for the design of optimal FE meshes.

The numerical results of the NP–P–S scheme can be readily used to post-compute ion fluxes through the pores. This calculation is important when considering the application of membranes in a separation process. The ion flux through a pore is shown to be strongly dependent on both zeta potential and pore radius. This is an indication of the effects of overlapping double layers.
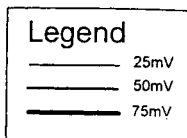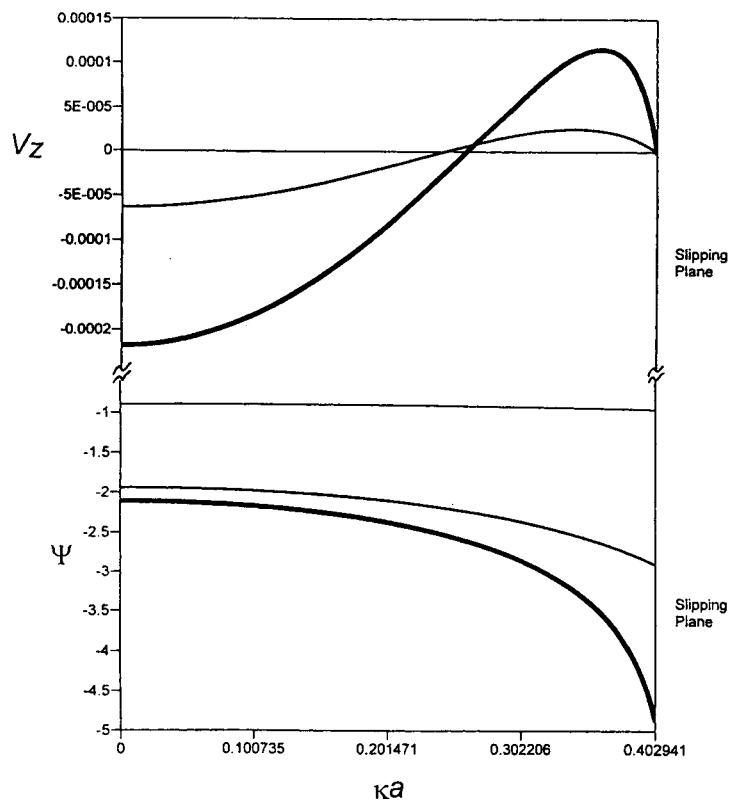
Figure 5. Dimensionless potential and axial velocity for $\zeta = -25, -50$ and -125 mV
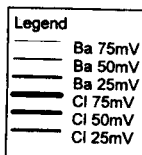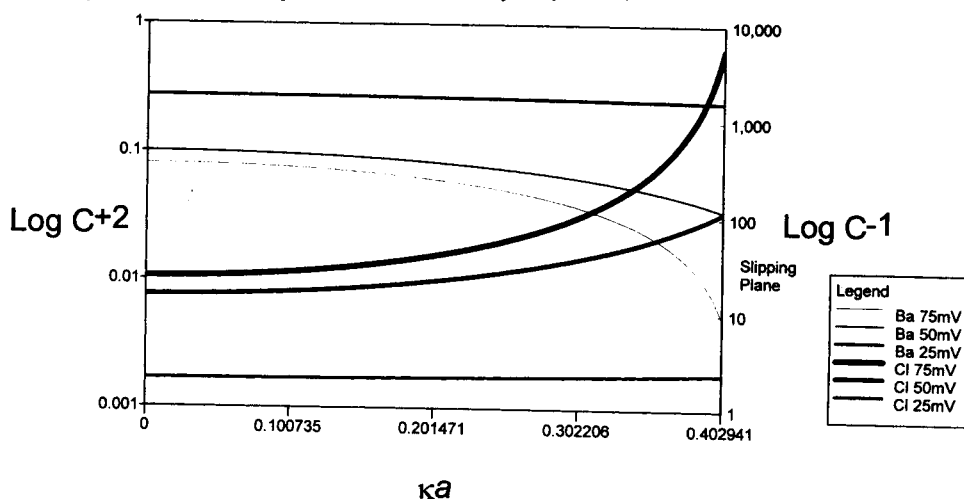
Figure 6. Dimensionless concentration profiles for $\zeta = -25, -50$ and -125 mV
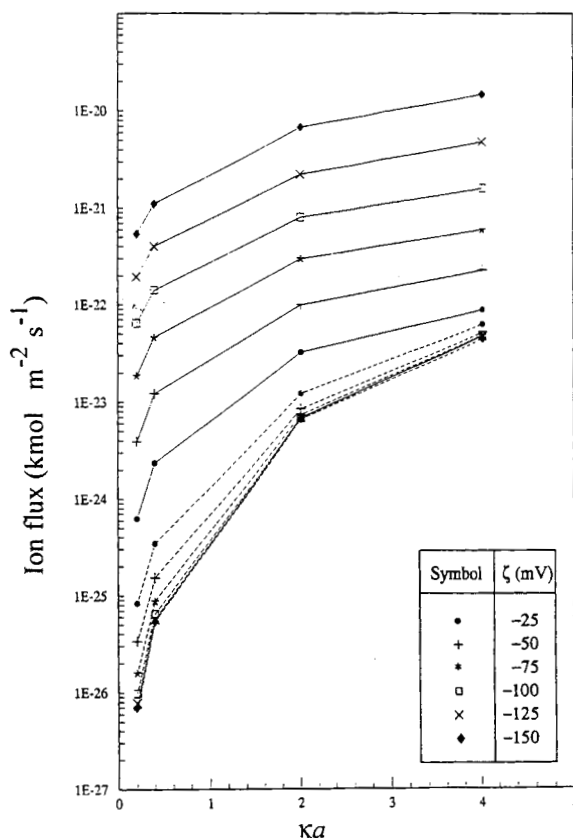
Figure 7. Ion flux as a function of κa for various values of ζ: solid lines, cation fluxes; broken lines, x-anion fluxes

REFERENCES

1. M. Mulder, *Basic Principles of Membrane Technology*, Kluwer, Dordrecht, 1991.
2. J. Hunter, *Zeta Potential in Colloid Science*, Academic, New York, 1981.
3. H. J. Verwey and T. Th. G. Overbeek, *Theory of the Stability of Lyophobic Colloids*, Elsevier, Amsterdam, 1948.
4. I. Dresner, 'Electrokinetic phenomena in charged microcapillaries', *J. Phys. Chem.*, **67**, 1635–1641 (1963).
5. F. A. Morrison and J. F. Osterle, 'Electrokinetic energy conversion in ultrafine capillaries', *J. Chem. Phys.*, **43**, 2111 (1965).
6. J. C. Fair and J. F. Osterle, 'Reverse electrodialysis in charged capillary membranes', *J. Chem. Phys.*, **54**, 3307–3316 (1971).
7. S. Levine, J. R. Marriott, G. Neale and N. Epstein, 'Theory of electrokinetic flow in fine cylindrical capillaries at high zeta-potentials', *J. Colloid Interface Sci.*, **52**, 136–149 (1975).
8. C. L. Rice and R. J. Whitehead, 'Electrokinetic flow in a narrow cylindrical capillary', *J. Phys. Chem.*, **69**, 4017–4024 (1965).
9. H. Oshima and K. Tamotsu, 'Electrokinetic flow between 2 parallel plates with surface charge layers', *J. Colloid Interface Sci.*, **135**, 443–448 (1990).
10. C. C. Christoforou, J. J. Westermann Clark and J. L. Anderson, 'The streaming potential and inadequacies of the Helmholtz equation', *J. Colloid Interface Sci.*, **106**, 1–11 (1985).
11. W. H. Koh and J. L. Anderson, 'Electroosmosis and electrical conductance in charged microcapillaries', *AIChE J.*, **21**, 1176 (1975).
12. J. L. Anderson, and W. H. Koh, 'Electrokinetic parameters for capillaries of different geometries', *J. Colloid Interface. Sci.*, **59**, 149–158 (1977).
13. A. E. James and D. J. A. Williams, 'Electrical double layer interaction energy for two cylinders', *J. Colloid Interface Sci.*, **79**, 33–46 (1981).
14. O. C. Zienkiewicz, *The Finite Element Method*, 3rd edn, McGraw-Hill, New York, 1977.
15. C. Taylor and P. Hood, 'Navier–Stokes equations using mixed interpolation', *Proc. Int. Conf. on FEM in Flow Problems*, 1974, pp. 121–132.

16. P. S. Huyakorn, C. Taylor, R. L. Lee and P. M. Gresho, 'A comparison of various mixed interpolation finite elements in the velocity–pressure formulations of the Navier–Stokes equations', *Comput. Fluids*, **6**, 25–35 (1978).
17. P. M. Gresho, R. L. Lee and R. L. Sani, 'On the time-dependent solution of the incompressible Navier–Stokes equations in two and three dimensions', in C. Taylor and K. Morgan (eds), *Recent Advances in Numerical Methods in Fluids*, Vol. 1, Pineridge, Swansea, 1980, pp. 27–79.
18. C. Taylor, J. Rance and J. O. Medwell, 'A note on the imposition of traction boundary conditions when using the FEM for solving incompressible flow problems', *Commun. Appl. Numer. Methods*, **1**, 113–121 (1985).
19. A. E. James and D. J. A. Williams, 'Numerical solution of the Poisson–Boltzmann equation', *J. Colloid Interface Sci.*, **107**, 44–59 (1985).
20. M. Abramowitz and I. A. Stegun, *Handbook of Mathematical Functions with Formulas, Graphs and Mathematical Tables*, United States National Bureau of Standards/Wiley, New York, 1964.
21. C. E. Thomas, 'Analysis of confined turbulent flows', *Ph.D. Thesis*, University of Wales, Swansea, 1982.
22. W. R. Bowen, Department of Chemical Engineering, University College of Swansea, personal communication, 1992.